Planetary and Space Science 75 (2013) 136–147

Contents lists available at SciVerse ScienceDirect

Planetary and Space Science

journal homepage: www.elsevier.com/locate/pss

Constraints on Titan's middle atmosphere ammonia abundance from Herschel/SPIRE sub-millimetre spectra ☆

N.A. Teanby [a,*], P.G.J. Irwin [b], C.A. Nixon [c], R. Courtin [d], B.M. Swinyard [e,f], R. Moreno [d], E. Lellouch [d], M. Rengel [g], P. Hartogh [g]

[a] School of Earth Sciences, University of Bristol, Wills Memorial Building, Queen's Road, Bristol BS8 1RJ, UK
[b] Atmospheric, Oceanic & Planetary Physics, Department of Physics, University of Oxford, Clarendon Laboratory, Parks Road, Oxford OX1 3PU, UK
[c] NASA Goddard Space Flight Center, Greenbelt, MD, USA
[d] LESIA-Observatoire de Paris, CNRS, Université Paris 6, Université Paris-Diderot, 5 place Jules Janssen, 92195 Meudon, France
[e] RAL Space, Science & Technology Facilities Council, Rutherford Appleton Laboratory, Chilton Didcot OX11 0QX, UK
[f] Physics and Astronomy Department, University College London, Gower Street, London WC1E 6BT, UK
[g] Max-Planck-Institut für Sonnensystemforschung, Max-Planck-Str. 2, 37191 Katlenburg-Lindau, Germany

ARTICLE INFO

Article history:
Received 18 September 2012
Received in revised form
16 November 2012
Accepted 19 November 2012
Available online 29 November 2012

Keywords:
Titan
Atmosphere
Composition
Photochemistry
Herschel
Sub-millimetre

ABSTRACT

Sub-millimetre spectra measured with Herschel's SPIRE Fourier Transform Spectrometer were used to search for ammonia (NH_3) in Titan's stratosphere. Observations were taken during 2010 and 2011, just after Titan's northern spring equinox, which occurred in mid-2009. In our analysis we used high spectral resolution data (0.074 cm^{-1} apodised) from the SPIRE shortwave spectrometer array (SSW), which provided the best possible signal-to-noise ratio for detecting any NH_3 emission features. These data have the most sensitivity to NH_3 spectral emission of any currently available observations, although despite this we did not detect any significant emission features above the noise. However, we can place an improved 3-sigma upper limit on NH_3 abundance of <0.19 ppb for altitudes 65–110 km (75 km peak sensitivity), or alternatively a column abundance of $<1.23\times10^{15}$ molecules/cm^2. These observations provide modest constraint for future photochemical models and are consistent with most current stratospheric predictions. Scaling of photochemical model profiles, in order to fit elevated abundances observed at 1100 km by Cassini's INMS instrument, are for the most part also consistent with our observations.

1. Introduction

Titan, Saturn's largest moon, is unusual because it has a thick nitrogen and methane atmosphere (1.5 bar surface pressure). Interaction with solar UV photons and magnetospheric electrons in Titan's upper atmosphere creates nitrogen and methane radicals, which form the basis of a rich photochemical cycle - producing a vast array of hydrocarbon and nitrile species (Wilson and Atreya, 2004; Lavvas et al., 2008; Krasnopolsky, 2009). These photochemical processes lead to the creation of complex organic molecules.

An essential element in understanding Titan's complex atmosphere is accurate measurement of trace species abundances at different atmospheric levels, which provide stringent constraints on active chemical pathways. Recently the Cassini–Huygens mission has played a critical role in unlocking the complexity of Titan's chemical inventory. Many new compounds have been discovered in the very upper layers of the atmosphere (>950 km altitude) using Cassini's Ion and Neutral Mass Spectrometer (INMS) (Waite et al., 2005; Vuitton et al., 2009), which samples gas for *in situ* analysis on each close flyby.

Deep within Titan's atmosphere, in the stratosphere and mesosphere (100–500 km altitude), remote sensing techniques currently provide the most complete information on atmospheric composition. For example, in the sub-millimetre, recent Herschel observations have lead to the discovery of HNC (Moreno et al., 2011), abundance determinations of CO, HCN and their isotopologues (Courtin et al., 2011), and water vapour vertical profiles (Moreno et al., 2012). At shorter wavelengths, in the far- and mid-infrared, which contain many more gas emission features, Cassini's Composite InfraRed Spectrometer (CIRS) has been very successful at measuring the detailed altitude and latitude distribution of major trace species (Flasar et al., 2005; Coustenis et al., 2007, 2010; de Kok et al., 2007a; Nixon et al., 2009;

* Corresponding author. Tel.: +44 117 3315006.
E-mail address: n.teanby@bristol.ac.uk (N.A. Teanby).

☆ *Herschel* is an ESA space observatory with science instruments provided by European-led Principal Investigator consortia and with important participation from NASA.

0032-0633/$ - see front matter © 2012 Elsevier Ltd. All rights reserved.
http://dx.doi.org/10.1016/j.pss.2012.11.008

Teanby et al., 2006b, 2007, 2008a,b, 2009b,a, 2010a; Vinatier et al., 2007, 2010; Cottini et al., 2012). However, the CIRS spectral resolution and sensitivity has so far been too low to detect emission features from any of the new species discovered at much higher altitudes by INMS. See for example Nixon et al. (2010) who used CIRS to determine upper limits for H_2CO, CH_3OH, CH_3CN, C_3H_4 (allene isomer), and NH_3. The abundance of many important molecules, including NH_3, is thus currently unconstrained in the middle atmosphere.

To further our understanding of Titan's atmosphere it is now critical to link the chemistry of the upper atmosphere (above 1000 km) to that of the stratosphere and mesosphere (100–500 km), which contain the majority of Titan's trace gas inventory. One of the key molecules for providing this link is ammonia (NH_3), which was measured with a volume mixing ratio (VMR) of 7×10^{-6} by INMS at 1100 km (Vuitton et al., 2007, 2009). A major deficiency of current chemical schemes is that the NH_3 abundance at this altitude is underestimated by orders of magnitude: Wilson and Atreya (2004) predict 4×10^{-8} at 1100 km (175 times less the observed); and Lavvas et al. (2008) and Krasnopolsky (2009) both predict around 2×10^{-7} at 1100 km (35 times less). Therefore, the mechanism for NH_3 production in Titan's atmosphere would appear to be much more efficient than current schemes can explain.

Current photochemical models produce high altitude (1100 km) NH_3 by electron recombination with NH_4^+ ions. However, recently Yelle et al. (2010) hypothesised that disagreement between models and the INMS observations could be caused by a previously neglected NH_3 production pathway: $NH_2 + H_2CN \rightarrow NH_3 + HCN$, which they propose is the dominant NH_3 source at high altitude.

In the stratosphere and mesosphere NH_3 is expected to be supplied via transport from high altitudes by vertical mixing processes. Hence, increased production at higher altitude should imply an increase in NH_3 at lower atmospheric levels also, which can be searched for using NH_3 sub-millimetre emission lines. There is also a possible local stratospheric source of NH_3 from cosmic ray induced dissociation of molecular nitrogen, which could lead to a local maximum in NH_3 abundance in the stratosphere (see e.g. Lavvas et al., 2008). Measurements of C_2N_2 (Teanby et al., 2009a) suggest that cosmic rays may indeed play an important role in Titan's stratospheric chemistry. However, stratospheric and mesospheric predictions of NH_3 abundance from the different published models vary by over two orders of magnitude and are not well constrained by current observations.

NH_3 has so far not been observed spectroscopically at all, and the best previously available stratospheric upper limit of 1.3×10^{-9} (Nixon et al., 2010) is too large to differentiate between possible photochemical models, which currently predict relative stratospheric abundances of order 10^{-10} or less (e.g. Lavvas et al., 2008). In this paper we use high sensitivity sub-millimetre observations by Herschel's SPIRE Fourier Transform Spectrometer (FTS) instrument to search for NH_3 in Titan's lower stratosphere in an attempt to provide improved constraints on photochemical pathways.

2. Observations

Observations were taken with the Herschel Space Observatory's (Pilbratt et al., 2010) SPIRE instrument (Griffin et al., 2010) as part of the HssO Key Program (Hartogh et al., 2009), just after Titan's mid-2009 northern spring equinox, between 22/6/2010 and 26/07/2011. The SPIRE FTS simultaneously observes a full spectrum from 14.6 to 51.8 cm^{-1} (685–193 μm) using two separate detector arrays to ensure maximum observing efficiency. The shortwave spectrometer array (SSW) covers 31.2–51.8 cm^{-1} and the longwave spectrometer array (SLW) covers 14.6–33.3 cm^{-1}. Observations were taken in high spectral resolution sparse pointed mode whereby the object is detected only in the central detector of each array and the whole spectrum is taken with a single spectral resolution. The nature of the detector spatial sampling, combined with Herschel's 3.5 m primary mirror, resulted in wavelength-dependent individual detector field-of-views of diameter $11-19''$ for the SSW and $18-40''$ for the SLW (Swinyard et al., 2010). Titan's disc typically had a solid-body diameter of $0.7''$ during these observations, resulting in disc-averaged spectra. The SSW spectra have the best signal-to-noise for our study as they cover the strongest NH_3 lines and have the least beam dilution because of their smaller field-of-view (FOV). It is these observations we concentrate on here. The SPIRE point observing mode sequences had total integrations between 22 min and 8 h 51 min. The total integration time was built up from multiple scans of the FTS mechanism, with each scan taking approximately 66 s. Following transformation to the spectral domain, the integrated spectrum from each observation sequence was formed by co-addition of the individual spectra. Observation properties are listed in Table 1. Five observations were taken in total, but we only use four of these in this paper – the first observation is not used because of its short integration time and contamination from Saturn. Fig. 1 shows the observing geometry and Titan's orientation during the four observation sequences.

Our analysis started with unapodised Level 2 data from the Herschel Science Archive (HSA), which are calibrated against the continuum spectrum of Uranus (Swinyard et al., 2010). Data had a sample spacing of 0.01 cm^{-1} and a native resolution comprising a sinc instrument function with a full-width half-maximum (FWHM) of 0.048 cm^{-1}. These data were apodised using a Hamming instrument function with a FWHM of 0.07373 cm^{-1} to remove the effects of ringing around gas emission peaks. This choice provided the best compromise between reducing ringing and maintaining the narrow widths of gas peaks. Apodised spectra (Fig. 2) show a very clean signal with minimal noise

Table 1
Details of the SSW observations used in this paper. Sub-Herschel point is given for observation mid-point. Shift is wavenumber correction applied to observation to give the best match to the reference spectrum. All spectra cover a wavelength range of 31.2–51.8 cm^{-1} with an unapodised/apodised spectral resolution of 0.048/0.07373 cm^{-1}.

Observations	Product ID	Start time (UT)	Integration time (s)	Sub-Herschel point		Shift (cm^{-1})
				Longitude (°W)	Latitude (°N)	
S0[a]	1342198925	2010-06-22 12:11:54	1322	273.58	2.05	–
S1	1342201495	2010-07-16 03:44:14	31 878	89.43	2.73	+0.0013
S2	1342224755	2011-07-25 23:38:55	10 786	235.65	8.09	+0.0042
S3	1342224756	2011-07-26 02:38:55	10 786	260.99	8.13	+0.0041
S4	1342224757	2011-07-26 05:38:55	10 786	263.80	8.13	+0.0045

[a] Observation on 22/6/2010 was not used due to contamination from Saturn and low signal-to-noise.

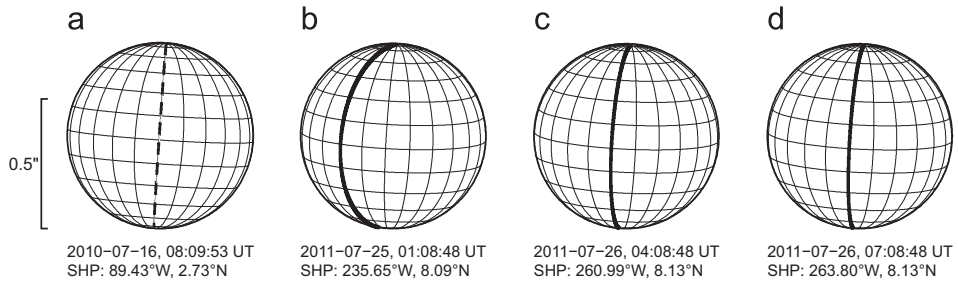

Fig. 1. Viewing geometry of Titan for the four observations analysed in this paper. Date and time are for observation mid-point. SHP is the longitude and latitude of the sub-Herschel point. Solid bold line indicates the 270°W meridian and bold dashed line indicates the 90°W meridian (0°W is the sub-Saturn direction).

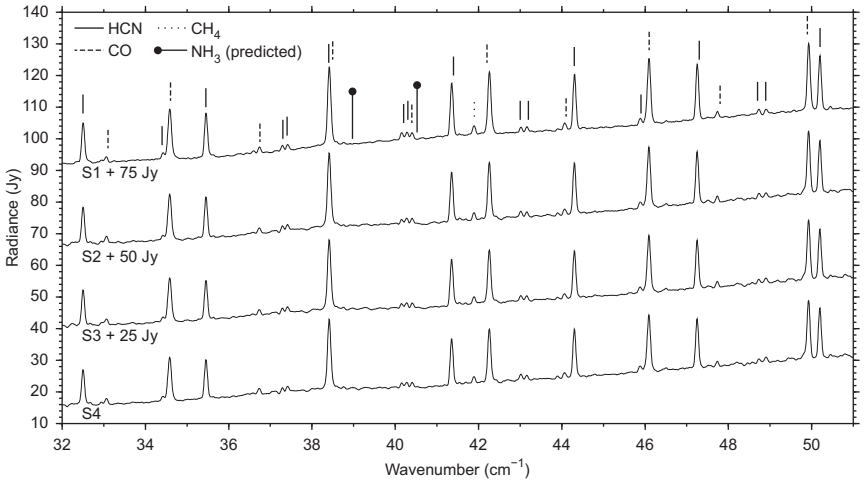

Fig. 2. Level 2 processed SSW spectra after convolution with a Hamming apodisation function with a FWHM of 0.07373 cm^{-1} for the four SPIRE observations. Spectra are offset vertically for clarity as indicated. The positions of emission features from CO, HCN, and CH_4 are indicated with vertical ticks. The predicted position of NH_3 lines are indicated by vertical ticks with blobs on. Note all visible emission peaks are accounted for by previously detected species.

features, although some slight continuum ripples are present due to residual instrumental effects. Initially we used the nominal error bar from the HSA, which was calculated using the standard deviation of the multiple scans taken to build up the total integrated spectrum. These errors were further refined during the analysis (Section 3.5).

3. Modelling and further data reduction

Our study is focussed on searching for very faint NH_3 spectral lines. Therefore, our main concern is defining realistic error bars and achieving an accurate continuum level so that any small features can be identified. The observed spectra contain superimposed ripples, which are instrument artifacts and not associated with Titan's spectrum. These must be removed before analysis can proceed. Commonly such artifacts are dealt with by modelling the line-to-continuum ratio. However, in this paper we chose to preserve the physical radiance units, which has the advantage of providing an additional check on the data calibration and model accuracy, in addition to being more intuitive to analyse.

In the wavelength region covered by the SSW, Titan's spectrum is affected by tropopause and lower stratospheric temperature, collision-induced absorption of N_2–CH_4–H_2 pair combinations, emission lines from isotopologues of CO, HCN, and to a lesser extent CH_4, and minimally by stratospheric haze. All these properties are well constrained by the Cassini CIRS instrument (Flasar et al., 2004, 2005) and the Huygens descent probe HASI (Fulchignoni et al., 2005) and GCMS instruments (Niemann et al., 2010), allowing a reliable synthetic spectrum to be generated for comparison with the SPIRE observations.

The aim of the remainder of this section is to use realistic baseline synthetic reference spectra to identify and remove ripples, leaving a cleaned spectrum suitable for identification of any small NH_3 features. This procedure comprises the following steps:

3.1. Conversion of radiance units

Spectra from the SPIRE Level 2 calibration pipeline have units of Janskys – the natural unit for unresolved point sources (Wilson et al., 2009) – where 1 Jy = 10^{-26} $W/m^2/Hz$. However, to correctly model Titan's disc-averaged spectra and account for varying emission angle, it is necessary to consider the spatial distribution of radiance, so units of spectral radiance $W/cm^2/sr/cm^{-1}$ are a more convenient working unit. To convert between the two units we must define the solid angle over which the emission takes place. For a solid body this would be simply defined from the cross-sectional area of the object. However, emission from the limb of Titan's extended atmosphere is significant well above its solid surface. This emission can be assumed to drop to zero at a radius of 3000 km for sub-millimetre wavelengths (Appendix A). Therefore, to obtain a disc-averaged spectral radiance, we assumed uniform emission over a circular area centred on Titan, with a radius of r=3000 km. The exact choice of r is not critical so long as it is large enough to include all of Titan's emission.

Consider a planet emitting over a circular area of radius r, a distance R from the observer. The solid angle Ω subtended by

the planet is given by

$$\Omega = \pi \frac{r^2}{R^2} \quad (1)$$

Dividing Janskys by Ω gives us units of spectral radiance 10^{-26} W/m^2/sr/Hz. To convert these units to the more standard W/cm^2/sr/cm^{-1} we must multiply by $10^{-26} \times c \times 10^{-4}$, where $c = 2.99792458 \times 10^{10}$ cm/s is the speed of light – 10^{-26} converts into Watts, 10^{-4} converts m^{-2} into cm^{-2}, and c converts frequency to wavelength.

The overall conversion is thus:

$$1\ \text{Jy} = 10^{-30} \frac{cR^2}{\pi r^2}\ \text{W/cm}^2\text{/sr/cm}^{-1} \quad (2)$$

3.2. Forward modelling of the SSW spectra

Synthetic reference spectra were created using the Nemesis retrieval tool (Irwin et al., 2008), which assumes a spherically symmetric atmosphere and uses the correlated-k approximation (Lacis and Oinas, 1991) for computational efficiency. Previously, we have used this code extensively to model Titan's spectrum (e.g. Teanby et al., 2010c, and references therein).

Gas spectroscopic data were based on the HITRAN database (Rothman et al., 2005) with the following modifications: CH_4 line intensities were revised after Wishnow et al. (2007); and HCN linewidths were modified for N_2 broadening as explained in Teanby et al. (2010b). Tables of absorption coefficients –or k-tables were created from the spectroscopic data and incorporated the Hamming instrument function directly in order to improve computational efficiency and to provide the best match to observations. The partition functions were calculated using a third order polynomial fit to the total partition function data in Fischer et al. (2003) (supplied with the HITRAN database) over the range 70–300 K. Collision-induced absorption from pairwise combinations of N_2, CH_4, and H_2 were calculated according to Borysow and Frommhold (1986a,b,c, 1987), Borysow (1991), and Borysow and Tang (1993). The wavenumber dependence of the main haze relative absorption cross section was determined from the volume absorption coefficients in Anderson and Samuelson (2011). The values we used are given in Table 2.

A reference atmosphere was then defined with composition, aerosol, and temperature profiles based on previous work. The assumed haze vertical profile was a simplified version based on results from CIRS (de Kok et al., 2007b, 2010) and Huygens/DISR (Tomasko et al., 2008) (Fig. 6). This profile was scaled such that the specific particle density was 3.9×10^{-2} particles/g at 150 km. This scaling gave a specific absorption of 3.9×10^{-2} particles/g $\times$ 1.26×10^{-3} cm^2/particle $= 4.9 \times 10^{-5}$ cm^2/g for an altitude of 150 km at 160 cm^{-1}, in agreement with Anderson and Samuelson (2011) (their Fig. 10 at latitude 15°S). The calculated nadir optical depth using this profile at the centre of the SSW bandpass (42 cm^{-1}) was 2.4×10^{-3} (see also Table 2). For comparison, Titan's atmosphere is effectively opaque at these wavenumbers due to N_2–N_2 and N_2–CH_4 collision-induced absorption, with an optical depth of unity occurring around 50 km altitude. Therefore, aerosols have very slight influence on this spectral region, but were included for completeness. The atmospheric temperature profile was based on Flasar et al. (2005) (Fig. 6) and gas vertical profiles were based on: Niemann et al. (2010) (CH_4); de Kok et al. (2007a) (CO); and Teanby et al. (2010b) (HCN). These values can be considered representative of equatorial conditions at the time of our observations.

After defining the spectroscopic parameters and reference atmosphere we calculated a Titan reference spectrum. To allow for differing emission angles and limb emission across Titan's disc, we created a disc-averaged spectrum based on 21 field-of-view points (Teanby and Irwin, 2007) using the procedure outlined in Appendix A. This is directly comparable to the unit-converted spectra from Section 3.1. Fig. 3(a) shows observation S1 compared to the reference atmosphere synthetic. The agreement is very close and gives us confidence in both the Level 2 data calibration and forward model. The model was also cross-checked against an independent radiative transfer code (Courtin et al., 2011). Note the reference synthetic spectrum is based entirely on prior knowledge from Cassini and at this point is not fitted to the observations in any way.

3.3. Removal of continuum ripples

The close agreement between observed and reference synthetic spectra allows us to correct for continuum ripples by making minor adjustments to the observed radiances based on the residual between the two spectra. However, the gas peaks contain real differences due to unmodelled spatial variations in temperature and composition over Titan's globe. Therefore, before estimating the continuum ripples the gas peaks must be masked out. To create a spectral mask we created a second reference spectrum with HCN, CO, and CH_4 rotational emission lines removed, and differenced this with the original reference spectrum. Any wavenumbers where the two spectra differed by more than 0.1 nW/cm^2/sr/cm^{-1} were considered to be influenced by HCN/CO/CH_4 emission and were masked out. Fig. 3(b) shows the reference spectra with gas peaks masked out - this allows the continuum ripples to be seen very clearly. Fig. 3(c) shows the residuals between observation and masked reference spectra, which has an amplitude of a few nW/cm^2/sr/cm^{-1}.

To use the residuals to remove the ripples we must first apply some smoothing and interpolation to: (1) allow correction of the continuum where gas lines exist; and (2) to avoid removing any narrow gas features from unmodelled trace species such as NH_3. To this end we fit a cubic b-spline curve with a knot spacing of 1.25 cm^{-1} (total spline width of 5 cm^{-1}) using the method of Teanby (2007) and remove this smoothed continuum residual from the observed spectra. Narrow gas lines will be unaffected by this procedure but if any real unmodelled broad features exist in the measurements they will be removed. This is unlikely, and in any case is not important for our purposes as any gas lines are much narrower than the knot spacing. The final ripple corrected spectrum is shown in Fig. 3(d). As the ripple position and amplitude changed for each observation, this process was performed individually for each of the four observed spectra.

3.4. Correction of wavelength scale

While modelling the spectra it was noticed that slight sub-sample scale wavenumber shifts existed in the observations.

Table 2
Relative absorption cross sections assumed for Titan's main haze as a function of wavenumber. τ is the integrated nadir column optical depth using the specific particle density profile in Fig. 6. The low optical depths show that haze has a very minor effect on Titan's spectrum at these wavelengths. While not covered by the SPIRE FTS, values at 160 cm^{-1} are also given to allow comparison with Anderson and Samuelson (2011).

Wavenumber (cm^{-1})	Cross section (cm^2/particle)	τ
30	1.30×10^{-10}	1.6×10^{-9}
35	6.18×10^{-05}	7.5×10^{-4}
40	1.59×10^{-04}	1.9×10^{-3}
45	2.65×10^{-04}	3.2×10^{-3}
50	4.61×10^{-04}	5.6×10^{-3}
55	6.13×10^{-04}	7.5×10^{-3}
[160	1.26×10^{-03}	1.5×10^{-2}]

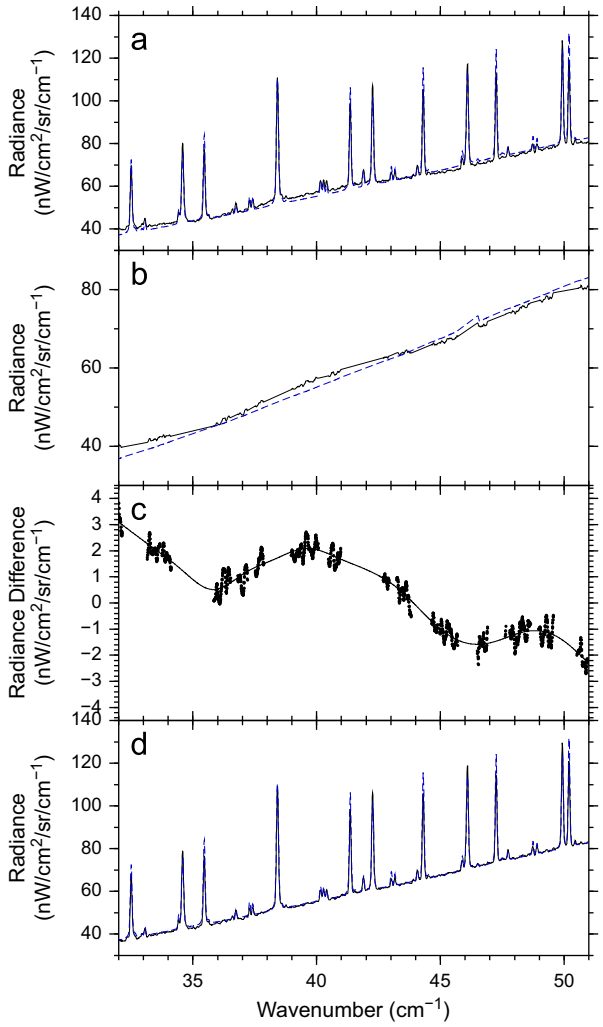

Fig. 3. Illustration of baseline ripple removal procedure for observation S1. (a) Observed spectrum (solid line), after conversion to spectral radiance, compared with the synthetic reference spectrum (dashed blue line) generated based on Cassini constraints. Overall agreement is excellent considering no fitting has been attempted at this stage, (b) observed continuum level (solid line) compared to reference spectrum (dashed blue line) after masking out gas emission peaks and (c) residual between observation and reference spectrum (points) and best fitting spline curve (solid line). Small but significant continuum ripples due to instrument artifacts are evident, (d) Comparison of reference spectrum (dashed blue line) with ripple corrected observation (solid line). Such ripple corrected spectra form the basis of our analysis. (For interpretation of the references to color in this figure caption, the reader is referred to the web version of this article.)

While small, these were very noticeable around the sharp gas peaks of HCN and CO. To correct for this, the reference synthetic spectrum was cross correlated with each observation to determine the shift magnitude and direction. The wavenumber grid was then shifted and the resulting spectrum linearly interpolated back onto the original wavenumber grid. Oversampling of the spectra was sufficiently fine that this did not introduce any interpolation artifacts (for example reduced peak heights). Shifts were all less than 0.005 cm^{-1} (Table 1) which is small compared to the 0.01 cm^{-1} sample spacing.

3.5. Creation of a final averaged spectrum

To maximise the signal-to-noise an average spectrum was created from the four individual de-rippled and wavelength corrected spectra S1–S4. This gave us an opportunity to improve the noise estimate on the spectrum using the standard deviation $\delta(v_j)$ between the four measured spectra $s_i(v_j)$ at wavenumbers v_j. Due to the small number of spectra, $\delta(v_j)$ will suffer from small number statistics and could be anomalously small, giving an unrealistically low value of the error for some wavenumbers. Therefore, to obtain a more accurate noise estimate, which can be used as a minimum measurement error at each wavenumber, we assume that the standard deviation is uniform across the whole spectral range. The standard deviation from all wavenumbers then provides a large number of independent estimates of the actual standard deviation, which can be combined to determine the sample mean standard deviation $\overline{\mu}$.

As standard deviation is restricted to positive numbers, the estimates $\delta(v_j)$ of $\overline{\mu}$ should be distributed log-normally (Forbes et al., 2011). In such a distribution the logarithm of the quantity is distributed normally and $\overline{\mu}$ can be estimated as follows.

Consider $M=4$ measured spectra $s_i(v_j)$ where $i=1\ldots M$ at N wavenumbers $v_j=1\ldots N$. The mean $\overline{s}(v_j)$ and standard deviation $\delta(v_j)$ at each wavenumber v_j are given by the usual equations for unweighted sample mean and standard deviation

$$\overline{s}(v_j)=\frac{\sum_{i=1}^{M} s_i(v_j)}{M} \tag{3}$$

$$\delta(v_j)=\sqrt{\frac{\sum_{i=1}^{M}(s_i(v_j)-\overline{s}(v_j))^2}{M-1}} \tag{4}$$

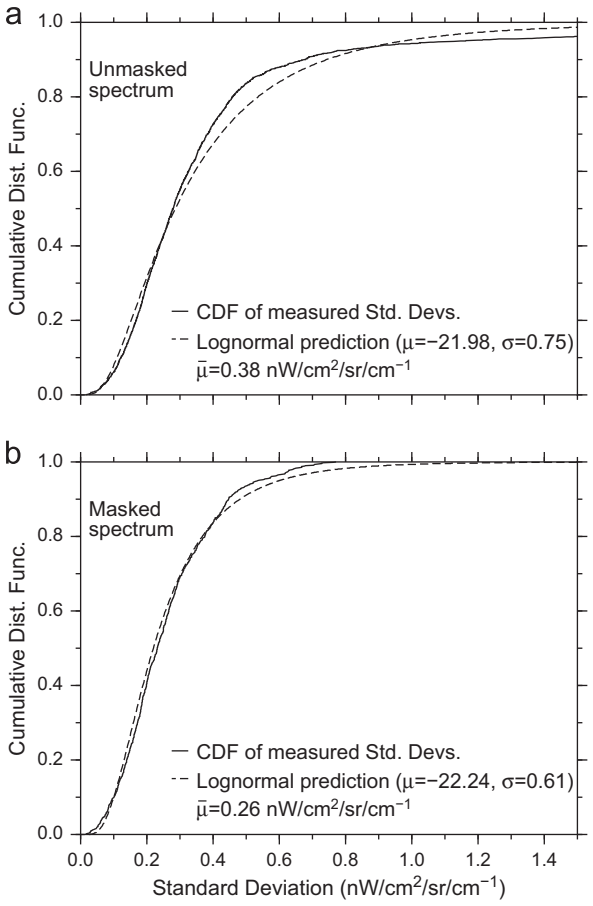

Fig. 4. Cumulative distribution function of standard deviations $\delta(v_j)$ between the four SSW observations (solid line) compared to theoretical log-normal distribution with parameters $\mu=$ mean(ln δ) and $\sigma=$ standard deviation (ln δ). $\overline{\mu}$ is the equivalent mean value of the standard deviation corresponding to the plotted log-normal predicted CDF. (a) Distribution for all wavenumbers, indicating a tail of high standard deviations in the observed spectra and (b) distribution of continuum-only wavenumbers, which matches the theoretical distribution very well – suggesting $\overline{\mu}$ is a representative standard deviation for our observations.

If $\delta(v_j)$ is distributed log-normally, the cumulative distribution function (CDF) is given by

$$P(\delta \le x|\mu,\sigma) = \frac{1}{\sigma\sqrt{2\pi}}\int_0^x \frac{\exp(-(\ln t-\mu)^2/2\sigma^2)}{t}\,dt \quad (5)$$

where t is a dummy variable, and μ and σ are the mean and standard deviation of the logged distribution $\ln\delta$ (Forbes et al., 2011). The corresponding mean $\overline{\mu}$ of the un-logged distribution is given by

$$\overline{\mu} = \exp\left(\mu + \frac{\sigma^2}{2}\right) \quad (6)$$

Parameters μ and σ of the log-normal distribution can be trivially calculated from the N values of $\ln\delta(v_j)$, and the equivalent mean standard deviation $\overline{\mu}$ calculated. If $\overline{\mu}$ is representative of the continuum standard deviation, then there should be good correspondence between observed and theoretical cumulative distribution function (CDF). Fig. 4(a) shows the distribution of standard deviation estimates $\delta(v_j)$ for the entire spectral range, along with the theoretical distribution calculated using Eqs. (5) and (6). This exhibits a mismatch between measured and theoretical log-normal CDFs, which is caused by a tail of high standard deviations. Inspection of the data showed that standard deviations of wavenumbers centred on the gas peaks were higher than those in the continuum regions. This is to be expected, as the slight differences in viewing geometry between observations cause more of the cold north polar region to come into view during later observations, which gives rise to systematic differences between the spectral peaks. Seasonal variations in Titan's atmosphere (Teanby et al., 2010c) could also have an effect. However, if the gas peaks are masked out, the agreement with the theoretical distribution is very good (Fig. 4b) – with $\overline{\mu}$ providing a reliable estimate of the actual continuum standard deviation. Therefore, as an overall conservative error estimate, we set a minimum standard deviation of $\overline{\mu} = 0.26\ \mathrm{nW/cm^2/sr/cm^{-1}}$ on the final combined average spectrum, in keeping with the estimate derived from continuum points, but if the calculated standard deviation for a particular wavenumber was larger than this, we used the larger value - i.e. the final error bar $\overline{\sigma}(v_j) = \max(\overline{\mu},\delta(v_j))$.

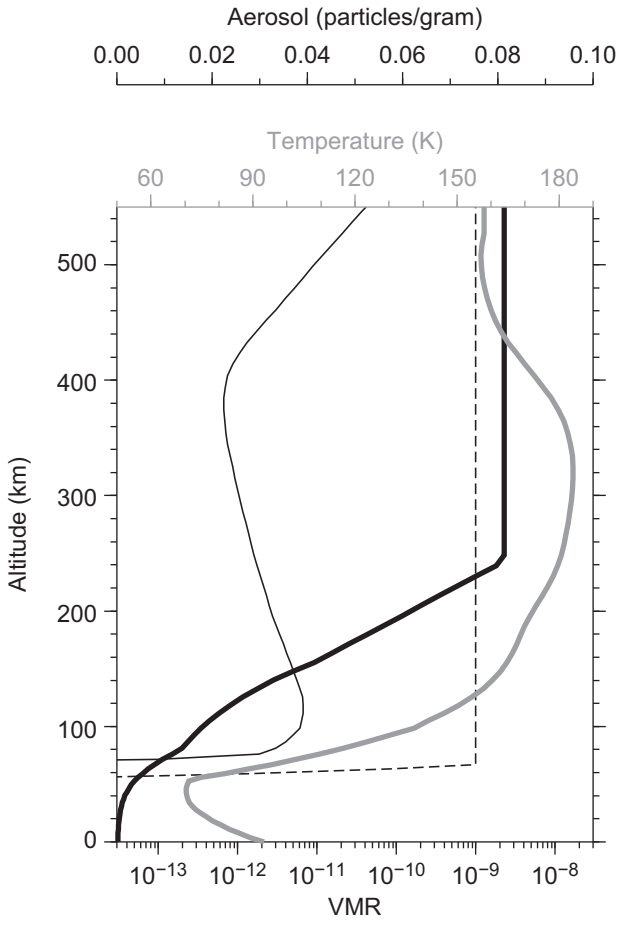

Fig. 6. NH_3 profiles assumed during our analysis. Thin solid line is the Lavvas et al. (2008) photochemical NH_3 profile; thin dashed line is the uniform NH_3 profile, which condenses around 60 km altitude; the thick black line is the aerosol profile; and the thick grey solid line shows the temperature profile assumed throughout from Flasar et al. (2005).

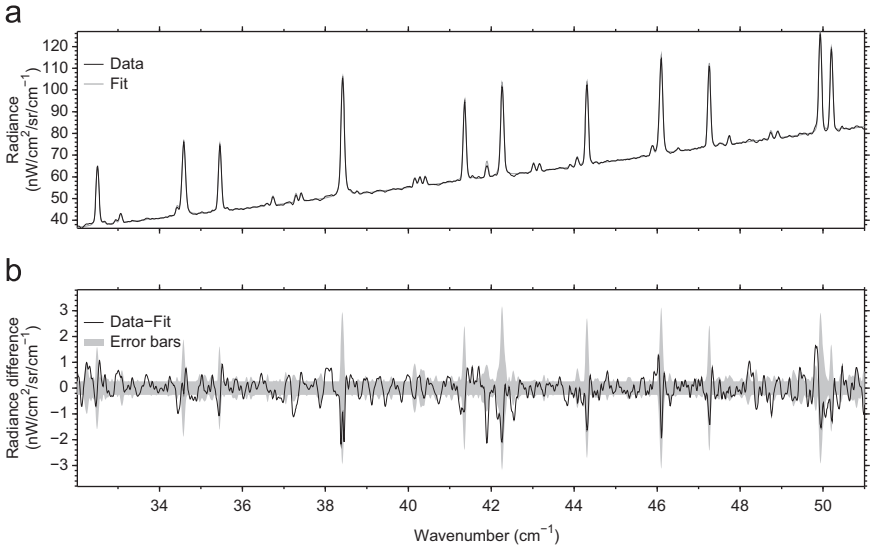

Fig. 5. (a) Final average of four wavenumber and ripple corrected spectra. The fit and observation are indistinguishable on this plot, (b) difference between average observed spectrum and fitted spectrum. Error bars $\overline{\sigma}(v_j)$ are shown with grey envelope and comprise the calculated standard deviation between the four observations $\delta(v_j)$, with a minimum value $\overline{\mu}$ set by the distribution fitted to the continuum standard deviation values in Fig. 4. Note that increases in standard deviation are coincident with gas emission peaks and are caused by slight changes in geometry throughout the observation period combined with the nonspherically symmetric nature of Titan's atmosphere.

The final averaged spectrum $\overline{s}(v_i)$ and error bar $\overline{\sigma}(v_i)$ are shown in Fig. 5 and is composed of the unweighted average of four SPIRE spectra that have each individually had ripples removed and been corrected for any slight wavenumber shifts. This final cleaned spectrum was used to determine a baseline model most appropriate for the disc-averaged spectra. The fit was obtained by adjusting HCN and CO abundance such that the misfit between data and synthetic was minimised. Optimal values of HCN and CO were 140 ± 20 ppb and 47 ± 7 ppm, respectively. CO abundance is consistent with previous disc-averaged CO results of 40 ± 5 ppm (Courtin et al., 2011) and space based determinations from CIRS of 47 ± 8 ppm (de Kok et al., 2007a) and 55 ± 6 ppm (Teanby et al., 2010b). HCN is spatially highly variable, but results are consistent with disc-resolved CIRS measurements that indicate abundances of 100–300 ppb at tropical latitudes (Teanby et al., 2010b). The agreement of our disc-averaged results with previous spatially resolved determinations from CIRS shows that our assumption of spherically symmetry has not adversely affected the composition results.

4. Calculation of upper limits

The averaged spectrum from the previous section forms the basis of our upper limit calculations. The misfit χ^2 between measured and modelled spectra for a given NH_3 abundance α is given by

$$\chi^2(\alpha) = \frac{\sum_{i=1}^{N} (\overline{s}(v_i) - f(v_i,\alpha))^2}{\overline{\sigma}^2(v_i)} \quad (7)$$

where $\overline{s}(v_i)$ is the measured spectrum with variance $\overline{\sigma}^2(v_i)$, and $f(v_i,\alpha)$ is the modelled spectrum. First, we take the best fitting model from the previous section and calculate the initial misfit $\chi^2(0)$. Second, we introduce a gradually increasing volume mixing ratio (VMR) of ammonia α to calculate the function $\chi^2(\alpha)$. If NH_3 emission features exist in the spectrum, the fit should be improved and $\chi^2(\alpha)$ will have a significant minimum at the best fitting abundance. If insufficient NH_3 is present to produce a detectable feature then no

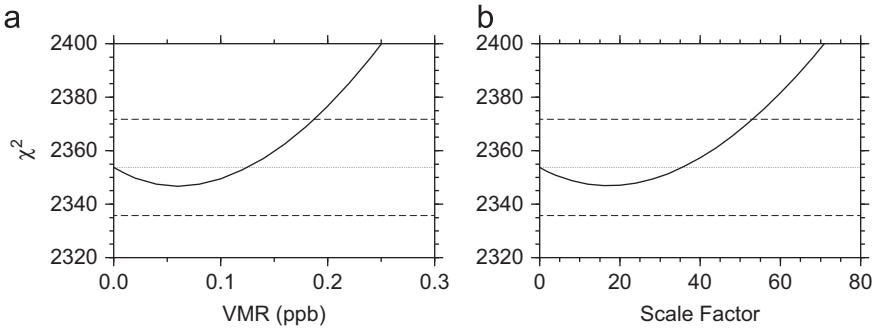

Fig. 7. Variation of model-observation misfit $\chi^2(\alpha)$ as a function of NH_3 abundance α. (a) $\chi^2(\alpha)$ for a vertical volume mixing ratio profile that is constant above the condensation level, (b) $\chi^2(\alpha)$ obtained by scaling the photochemical profile of Lavvas et al. (2008). Lower dashed lines indicate 3-sigma detection criteria – that are not attained in either case. Upper dashed line gives the 3-sigma upper limit threshold. Upper limits are 0.19 ppb for the constant profile and a scale factor of 53 for the scaled Lavvas et al. (2008) profile.

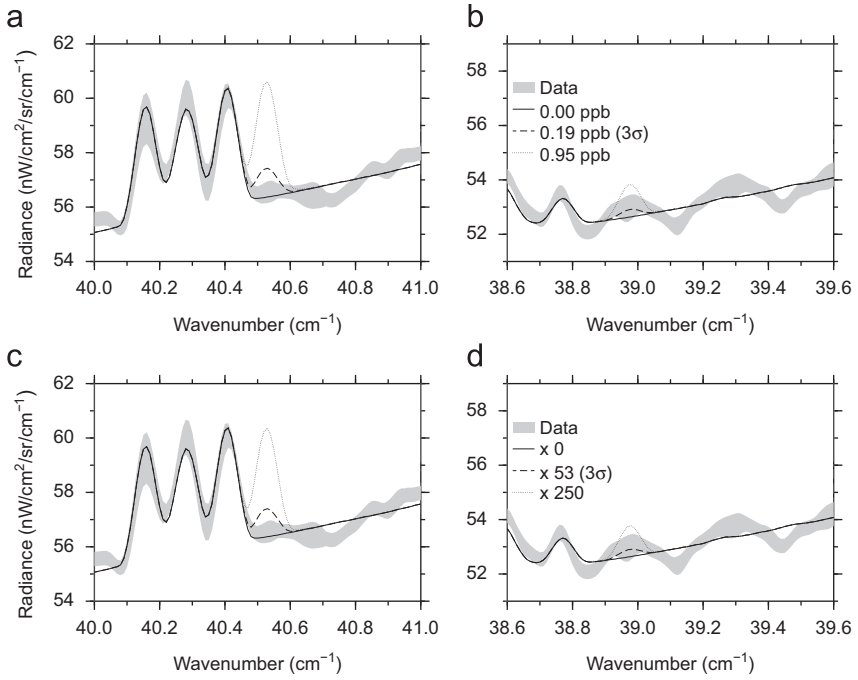

Fig. 8. Close-up of spectral windows containing the two strongest NH_3 features in the SSW range. Data and error bars are indicated with grey envelope and lines show synthetic spectra with: no NH_3 (solid); NH_3 at the 3-sigma level (dashed); and five times the 3-sigma level to illustrate the NH_3 peak positions (dotted). (a,b) Show the constant VMR profile case and (c,d) show the scaled Lavvas et al. (2008) photochemical profile case. No spectral emission from NH_3 is visible in the data above the noise in either case. The three emission lines between 40.10 and 40.45 cm^{-1} correspond to $HC^{15}N$, $C^{18}O$, and ^{13}CO, respectively.

significant minimum will exist and $\chi^2(\alpha)$ will increase. As we are adjusting a single variable (the NH_3 abundance), a 3-sigma upper limit would usually be defined as the point where χ^2 has increased by $3^2=9$ (Press et al., 1992). However, because the spectrum is oversampled by a factor of four, there is only one independent data point for every four. Therefore, the 3-sigma upper limit is defined when $\chi^2(\alpha)$ increases by $3^2*\sqrt{4}=18$ to $\chi^2(\alpha)=\chi^2(0)+18$. Similarly, a 3-sigma detection would require a reduction in $\chi^2(\alpha)$ of 18 to $\chi^2(\alpha)=\chi^2(0)-18$. Except for this modification for oversampling, this method is the same as Teanby et al. (2006a, 2009a).

The size of NH_3 spectral feature is somewhat dependent on the NH_3 vertical profile as well as its abundance. As this is currently unknown we explore two end member cases:

- *Uniform profile*: Where the volume mixing ratio is constant above the condensation level. Below the condensation level it is defined by the saturation vapour pressure, which at temperature T in Kelvin is given in atmospheres by $P_{svp}(T)=\exp(A+B/T+CT)$ with $A=22.70358$, $B=-4190.773$ K, $C=-0.2156661$ K^{-1} (based on Lide, 1995 data covering $T=160$–300 K). Re-evaporation of any condensate below the tropopause cold trap was suppressed to avoid unphysically high abundances in the troposphere.
- *Photochemical profile*: Where we used the photochemical profile of Lavvas et al. (2008). This profile was simply scaled to vary the abundance, but the VMR in the lower stratosphere was limited by the saturation vapour pressure equation above.

These profiles are shown in Fig. 6.

5. Results

Fig. 7 shows χ^2 as a function of NH_3 abundance for uniform and photochemical profile cases. Neither case has a minimum χ^2 below $\chi^2(0)-18$, implying that we do not detect NH_3 at the 3-sigma level with these data. Instead our data give 3-sigma upper limits (corresponding to $\chi^2(0)+18$) with a VMR of <0.19 ppb for the uniform profile and a scale factor of <53 for the scaled photochemical profile of Lavvas et al. (2008). The contribution functions at these kind of abundances peak at

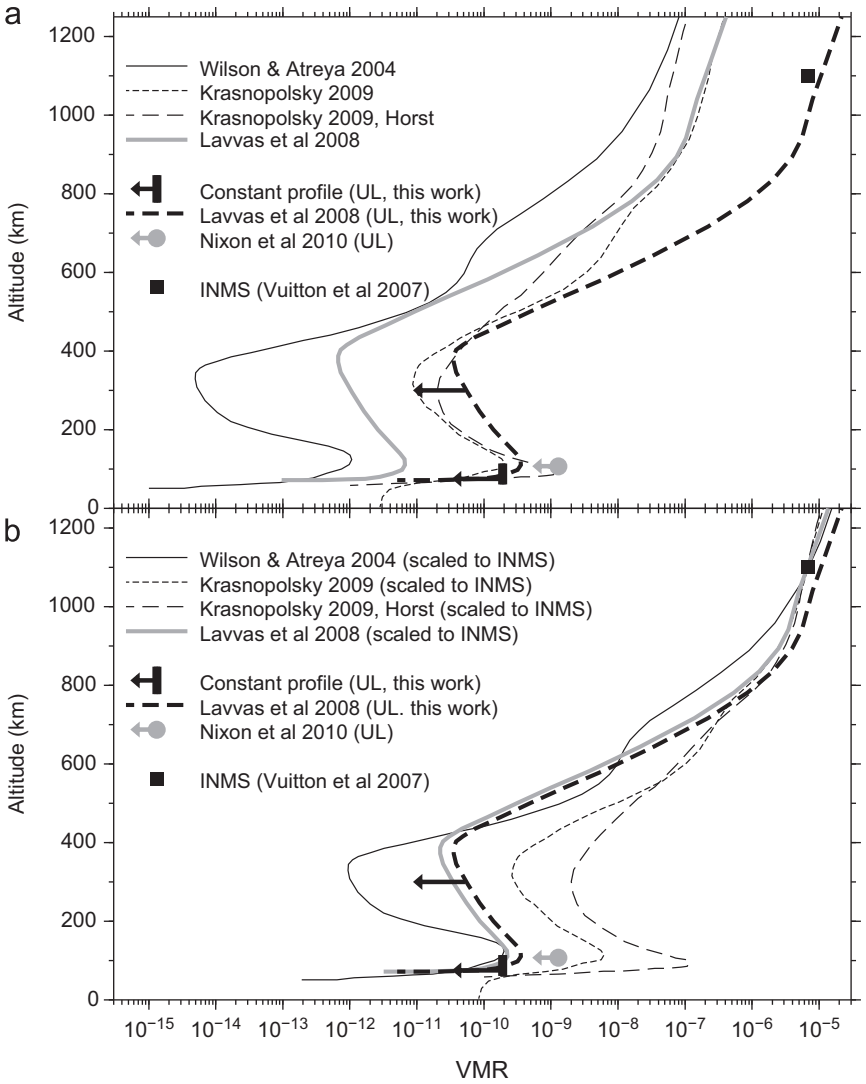

Fig. 9. Comparison of our derived NH_3 upper limits with predicted photochemical profiles from the literature. The previous best upper limit (UL) from Nixon et al. (2010) is also shown for comparison. (a) Direct photochemical model output. All photochemical profiles are consistent with our upper limit, except Krasnopolsky's case using the Hörst et al. (2008) eddy mixing profile (given in his Appendix A), (b) photochemical model output but rescaled to match the INMS measurement at 1100 km. In this case only the Lavvas et al. (2008) and Wilson and Atreya (2004) profiles are consistent with the data, although the assumption of linear scaling across 1000 km of atmosphere is unlikely to be representative of the full chemical complexity. Note that the secondary peaks at $\approx$ 100 km in the NH_3 photochemical model profiles are due to increased production related to cosmic rays.

75 km (FWHM between 65 and 110 km), so sound the lower stratosphere. Synthetic spectra, created assuming these upper limits, are shown in Fig. 8 for the spectral regions surrounding the two strongest NH_3 features. In addition to having no formal statistically significant abundance, a visual inspection of the spectra shows no observable NH_3 emission features above the noise.

6. Discussion and conclusions

The SPIRE data considered here give 3-sigma upper limits on Titan's stratospheric NH_3 of 0.19 ppb assuming a uniform profile, or 53 times the Lavvas et al. (2008) photochemical profile. These constraints are an order of magnitude better than the previous best upper limit of 1.3 ppb from Cassini CIRS (Nixon et al., 2010). This improvement is mainly a result of the factor of 10 improvement in spectral resolution obtained with SPIRE, while maintaining comparable noise levels to CIRS. Our values correspond to total column abundances of $<1.23\times10^{15}$ molecules/cm^2 (uniform) and $<0.94\times10^{15}$ molecules/cm^2 (photochemical), which is a relatively profile-independent measure. Therefore, the only current detection of NH_3 in Titan's atmosphere remains the in-situ measurement of 7×10^{-6} at 1100 km by Cassini INMS (Vuitton et al., 2007, 2009). If the Lavvas et al. (2008) profile is scaled by a factor of 33.5 to match the INMS value (as done by Lellouch et al., 2010), the resulting profile falls just below our upper limit so is still consistent with the SPIRE data.

Fig. 9(a) compares our results to available predicted NH_3 profiles from the literature (Wilson and Atreya, 2004; Krasnopolsky, 2009; Lavvas et al., 2008). While our new results provide a much improved constraint in the lower stratosphere, the only profile that can actually be ruled out based on our data is the supplemental case in Krasnopolsky (2009) which used the modified Hörst values (Hörst et al., 2008) for the eddy mixing profile. All other profiles fall below our upper limit at 75 km altitude.

If volume mixing ratio profiles are scaled in order to fit the INMS observation at 1100 km (Fig. 9(b)), then both Krasnopolsky (2009) profiles can be ruled out. However, the application of such a simple scaling is a gross oversimplification of the effect of increased NH_3 abundance at 1100 km and does not provide a rigourous test of the models. Therefore, the abundance of NH_3 in Titan's stratosphere remains an open question. Prospects for future detection of NH_3 in the sub-millimetre range remain promising, but will require an improvement in sensitivity of an order of magnitude or more before photochemical predictions can be tested further. Therefore, while our upper limit is the most stringent to date, we must await future missions to improve the accuracy and draw more insightful conclusions about Titan's ammonia cycle.

Acknowledgements

This work was funded by the UK Science and Technology Facilities Council and the Leverhulme Trust. SPIRE has been developed by a consortium of institutes led by Cardiff University (UK) and including Univ. Lethbridge (Canada); NAOC (China); CEA, LAM (France); IFSI, Univ. Padua (Italy); IAC (Spain); Stockholm Observatory (Sweden); Imperial College London, RAL, UCL-MSSL, UKATC, Univ. Sussex (UK); and Caltech, JPL, NHSC, Univ. Colorado (USA). This development has been supported by national funding agencies: CSA (Canada); NAOC (China); CEA, CNES, CNRS (France); ASI (Italy); MCINN (Spain); SNSB (Sweden); STFC (UK); and NASA (USA).

Appendix A. Radiative transfer modelling of a disc-averaged spectrum

Fig. A1 shows the spectral radiance emitted by Titan as a function of offset x from the sub-observer point, calculated using the reference atmosphere from Section 3.2. There is significant emission beyond Titan's solid body radius of 2575 km due to its extended atmosphere. This manifests itself as limb-brightening for both line and continuum emission.

Fig. A2 shows a synthetic Titan image based on the modelled radiances in Fig. A1. The SSW field of view diameter D is much larger than Titan's diameter, resulting in a disc-averaged spectrum. Figs. A1 and A2 show that all emission from Titan can be considered to originate from offsets of $x\le r$, where $r=3000$ km. In Section 3.1 we converted Janskys into a disc-averaged spectral radiance $\bar{s}$ assuming a circular emitting area with radius r. This is defined by

$$\bar{s}=\frac{\int_0^r\int_0^{2\pi} xs(x,\phi)\,d\phi\,dx}{\pi r^2} \tag{A1}$$

where $s(x,\phi)$ is the spectral radiance at offset x and azimuth ϕ on Titan's disc. Assuming a spherically symmetric planet gives rise to a radially symmetric radiance distribution across the disc, which results in the simplified form:

$$\bar{s}=\frac{\int_0^r 2\pi xs(x)\,dx}{\pi r^2} \tag{A2}$$

In the forward model $\bar{s}$ can be calculated as a weighted sum of P discrete field-of-view averaging points (Teanby and Irwin, 2007) with offsets x_i and calculated spectral radiances s_i. The problem is then to calculate the weights w_i to assign to each of these points, which we solve as follows.

The continuous form of Eq. (A2) for $\bar{s}$ can be approximated in the case of discrete radiance points by

$$\bar{s}\approx\frac{\sum_{i=1}^{P}\bar{s}_i\pi(x_{i+1}^2-x_i^2)}{\pi r^2} \tag{A3}$$

where $\bar{s}_i$ is area weighted mean spectral radiance for the annulus bounded by x_i and x_{i+1} (Fig. A2(b))

$$\bar{s}_i=\frac{\int_{x_i}^{x_{i+1}} 2\pi xs(x)\,dx}{\pi(x_{i+1}^2-x_i^2)} \tag{A4}$$

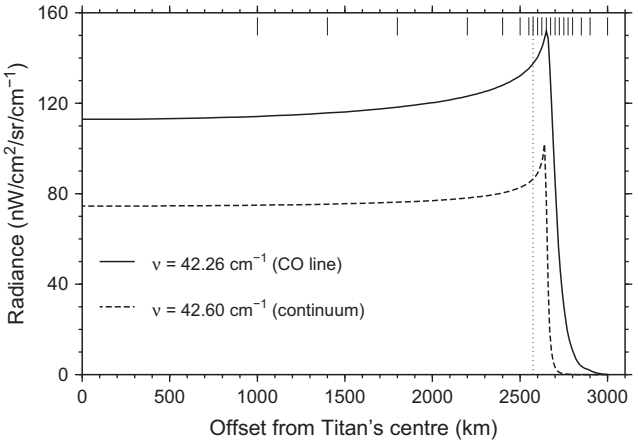

Fig. A1. Line and continuum spectral radiance profiles as a function of offset from Titan's centre. Significant emission takes place beyond the solid body radius at 2575 km. Vertical ticks indicate the location of FOV averaging points used to calculate the disc-averaged spectral radiance. Smaller spacing is required near the limb to capture the limb brightening effects.

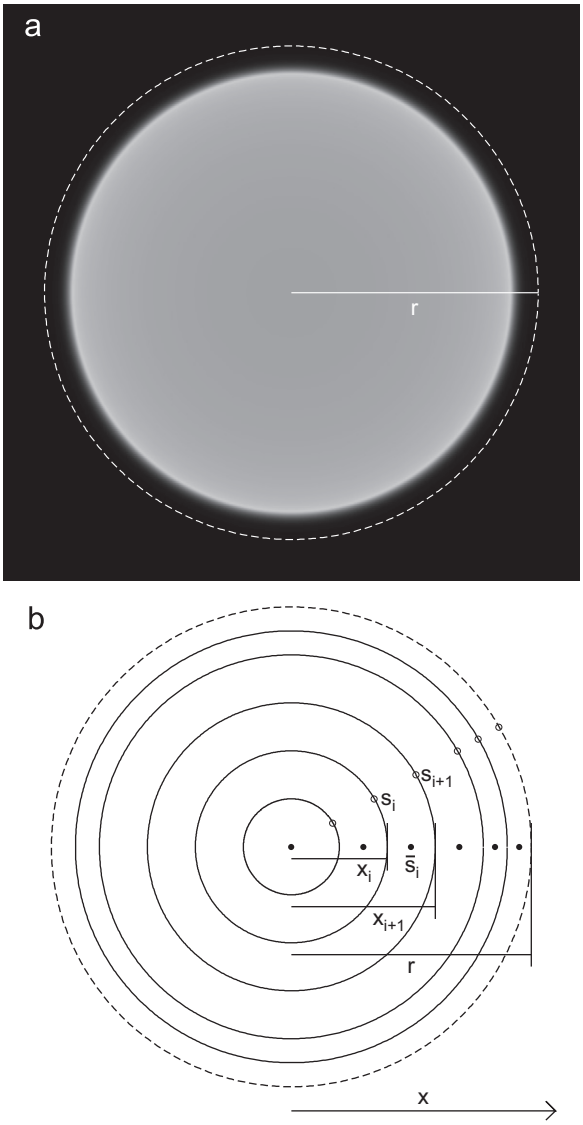

Fig. A2. (a) Synthetic image of Titan created using the CO line emission at 42.26 cm^{-1} in Fig. A1. Limb brightening is evident and emission drops to zero for $x > r$. Dashed line shows $r = 3000$ km. The SSW field of view is very large and subtends 11−19″ compared to Titan's 0.7″ diameter, so is not shown and (b) illustration of terminology used to define the disc-averaged spectral radiance. Titan is split into 21 unequal annuli with radii between 0 and $r = 3000$ km.

By assuming linear variation of $s(x)$ with offset x, the integral form can be replaced using the trapezium rule with

$$\bar{s}_i = \frac{2\pi(x_{i+1}-x_i)(x_i s_i + x_{i+1}s_{i+1})/2}{\pi(x_{i+1}^2 - x_i^2)} \quad \text{(A5)}$$

$$\bar{s}_i = \frac{(x_i s_i + x_{i+1}s_{i+1})}{(x_i + x_{i+1})} \quad \text{(A6)}$$

The total disc-averaged spectral radiance is then given by substitution into Eq. (A3)

$$\bar{s} \approx \frac{\sum_{i=1}^{P}(x_i s_i + x_{i+1}s_{i+1})(x_{i+1}-x_i)}{r^2} \quad \text{(A7)}$$

This expression can be expanded to give the FOV weights w_i for each discrete spectral radiance s_i:

$$w_1 = \frac{x_1 x_2 - x_1^2}{r^2} = 0 \quad \text{as } x_1 = 0 \quad \text{(A8)}$$

Table A1
Field of view averaging points used to produce the synthetic reference spectra. The weights w_i add up to unity.

i	x (km)	Tangent altitude (km)	Emission angle (°)	w_i
1	0	–	0.0	0.0
2	1000	–	22.85	0.15556
3	1400	–	32.94	0.12444
4	1800	–	44.35	0.16000
5	2200	–	58.69	0.14667
6	2400	–	68.75	0.08000
7	2500	–	76.14	0.04167
8	2550	–	82.01	0.02125
9	2575	0	90	0.01431
10	2600	25	90	0.01444
11	2625	50	90	0.01458
12	2650	75	90	0.01472
13	2675	100	90	0.01486
14	2700	125	90	0.01500
15	2725	150	90	0.01514
16	2750	175	90	0.01528
17	2775	200	90	0.01542
18	2800	225	90	0.02333
19	2850	275	90	0.03167
20	2900	325	90	0.04833
21	3000	425	90	0.03333

$$w_i = \frac{x_i x_{i+1} - x_{i-1}x_i}{r^2} \quad \text{(A9)}$$

$$w_P = \frac{x_P^2 - x_{P-1}x_P}{r^2} \quad \text{(A10)}$$

We found that 21 field of view averaging points were sufficient to accurately model the disc-averaged spectrum to within the measurement error. These points and their weights are given in Table A1.

References

Anderson, C.M., Samuelson, R.E., 2011. Titan's aerosol and stratospheric ice opacities between 18 and 500 μm: vertical and spectral characteristics from Cassini CIRS. Icarus 212, 762–778.

Borysow, A., 1991. Modelling of collision-induced infrared-absorption spectra of H_2–H_2 pairs in the fundamental band at temperatures from 20 K to 300 K. Icarus 92, 273–279.

Borysow, A., Frommhold, L., 1986a. Collision-induced rototranslational absorption spectra of N_2–N_2 pairs for temperatures from 50 to 300 K. Astrophysical Journal 311, 1043–1057.

Borysow, A., Frommhold, L., 1986b. Theoretical collision-induced rototranslational absorption spectra for modeling Titan's atmosphere: H_2–N_2 pairs. Astrophysical Journal 303, 495–510.

Borysow, A., Frommhold, L., 1986c. Theoretical collision-induced rototranslational absorption spectra for the outer planets: H_2–CH_4 pairs. Astrophysical Journal 304, 849–865.

Borysow, A., Frommhold, L., 1987. Collision-induced rototranslational absorption spectra of CH_4–CH_4 pairs at temperatures from 50 to 300 K. Astrophysical Journal 318, 940–943.

Borysow, A., Tang, C., 1993. Far infrared CIA spectra of N_2–CH_4 pairs for modeling of Titan's atmosphere. Icarus 105, 175–183.

Cottini, V., Nixon, C.A., Jennings, D.E., Anderson, C.M., Gorius, N., Bjoraker, G.L., Coustenis, A., Teanby, N.A., Achterberg, R.K., Bézard, B., de Kok, R., Lellouch, E., Irwin, P.G.J., Flasar, F.M., Bampasidis, G., 2012. Water vapor in Titan's stratosphere from Cassini CIRS far-infrared spectra. Icarus 220, 855–862.

Courtin, R., Swinyard, B.M., Moreno, R., Fulton, T., Lellouch, E., Rengel, M., Hartogh, P., 2011. First results of Herschel-SPIRE observations of Titan. Astronomy & Astrophysics 536, L2.

Coustenis, A., Achterberg, R.K., Conrath, B.J., Jennings, D.E., Marten, A., Gautier, D., Nixon, C.A., Flasar, F.M., Teanby, N.A., Bézard, B., Samuelson, R.E., Carlson, R.C., Lellouch, E., Bjoraker, G.L., Romani, P.N., Taylor, F.W., Irwin, P.G., Fouchet, T., Hubert, A., Orton, G.S., Kunde, V.G., Vinatier, S., Mondellini, J., Abbas, M.M., Courtin, R., 2007. The composition of Titan's stratosphere from Cassini/CIRS mid-infrared spectra. Icarus 189, 35–62.

Coustenis, A., Nixon, C., Achterberg, R., Lavvas, P., Vinatier, S., Teanby, N., Bjoraker, G., Carlson, R., Piani, L., Bampasidis, G., Flasar, F., Romani, P., 2010. Titan trace gaseous composition from CIRS at the end of the Cassini-Huygens prime mission. Icarus 207, 461–476.

Fischer, J., Gamache, R.R., Goldman, A., Rothman, L.S., Perrin, A., 2003. Total internal partition sums for molecular species in the 2000 edition of the HITRAN database. Journal of Quantitative Spectroscopy and Radiative Transfer 82, 401–412.

Flasar, F.M., Achterberg, R.K., Conrath, B.J., Gierasch, P.J., Kunde, V.G., Nixon, C.A., Bjoraker, G.L., Jennings, D.E., Romani, P.N., Simon-Miller, A.A., Bézard, B., Coustenis, A., Irwin, P.G.J., Teanby, N.A., Brasunas, J., Pearl, J.C., Segura, M.E., Carlson, R.C., Mamoutkine, A., Schinder, P.J., Barucci, A., Courtin, R., Fouchet, T., Gautier, D., Lellouch, E., Marten, A., Prange, R., Vinatier, S., Strobel, D.F., Calcutt, S.B., Read, P.L., Taylor, F.W., Bowles, N., Samuelson, R.E., Orton, G.S., Spilker, L.J., Owen, T.C., Spencer, J.R., Showalter, M.R., Ferrari, C., Abbas, M.M., Raulin, F., Edgington, S., Ade, P., Wishnow, E.H., 2005. Titan's atmospheric temperatures, winds, and composition. Science 308, 975–978.

Flasar, F.M., Kunde, V.G., Abbas, M.M., Achterberg, R.K., Ade, P., Barucci, A., Bézard, B., Bjoraker, G.L., Brasunas, J.C., Calcutt, S., Carlson, R., Esarsky, C.J.C., Conrath, B.J., Coradini, A., Courtin, R., Coustenis, A., Edberg, S., Edgington, S., Ferrari, C., Fouchet, T., Gautier, D., Gierasch, P.J., Grossman, K., Irwin, P., Jennings, D.E., Lellouch, E., Mamoutkine, A.A., Marten, A., Meyer, J.P., Nixon, C.A., Orton, G.S., Owen, T.C., Pearl, J.C., Prange, R., Raulin, F., Read, P.L., Romani, P.N., Samuelson, R.E., Segura, M.E., Showalter, M.R., Simon-Miller, A.A., Smith, M.D., Spencer, J.R., Spilker, L.J., Taylor, F.W., 2004. Exploring the Saturn system in the thermal infrared: the Composite Infrared Spectrometer. Space Science Reviews 115, 169–297.

Forbes, C., Evans, M., Hastings, N., Peacok, B., 2011. Statistical Distributions, 4th edition Wiley, Hoboken, New Jersey.

Fulchignoni, M., Ferri, F., Angrilli, F., Ball, A.J., Bar-Nun, A., Barucci, M.A., Bettanini, C., Bianchini, G., Borucki, W., Colombatti, G., Coradini, M., Coustenis, A., Debei, S., Falkner, P., Fanti, G., Flamini, E., Gaborit, V., Grard, R., Hamelin, M., Harri, A.M., Hathi, B., Jernej, I., Leese, M.R., Lehto, A., Stoppato, P.F.L., Lopez-Moreno, J.J., Makinen, T., McDonnell, J.A.M., McKay, C.P., Molina-Cuberos, G., Neubauer, F.M., Pirronello, V., Rodrigo, R., Saggin, B., Schwingenschuh, K., Seiff, A., Simoes, F., Svedhem, H., Tokano, T., Towner, M.C., Trautner, R., Withers, P., Zarnecki, J.C., 2005. In situ measurements of the physical characteristics of Titan's environment. Nature 438, 785–791.

Hartogh, P., Lellouch, E., Crovisier, J., Banaszkiewicz, M., Bensch, F., Bergin, E.A., Billebaud, F., Biver, N., Blake, G.A., Blecka, M.I., Blommaert, J., Bockelée-Morvan, D., Cavalié, T., Cernicharo, J., Courtin, R., Davis, G., Decin, L., Encrenaz, P., Encrenaz, T., González, A., de Graauw, T., Hutsemékers, D., Jarchow, C., Jehin, E., Kidger, M., Küppers, M., de Lange, A., Lara, L.M., Lis, D.C., Lorente, R., Manfroid, J., Medvedev, A.S., Moreno, R., Naylor, D.A., Orton, G., Portyankina, G., Rengel, M., Sagawa, H., Sánchez-Portal, M., Schieder, R., Sidher, S., Stam, D., Swinyard, B., Szutowicz, S., Thomas, N., Thornhill, G., Vandenbussche, B., Verdugo, E., Waelkens, C., Walker, H., 2009. Water and related chemistry in the solar system. A guaranteed time key programme for Herschel. Planetary & Space Science 57, 1596–1606.

Hörst, S.M., Vuitton, V., Yelle, R.V., 2008. Origin of oxygen species in Titan's atmosphere. Journal of Geophysical Research 113, E10006.

Irwin, P., Teanby, N., de Kok, R., Fletcher, L., Howett, C., Tsang, C., Wilson, C., Calcutt, S., Nixon, C., Parrish, P., 2008. The NEMESIS planetary atmosphere radiative transfer and retrieval tool. Journal of Quantitative Spectroscopy and Radiative Transfer 109, 1136–1150.

de Kok, R., Irwin, P.G.J., Teanby, N.A., Lellouch, E., Bezard, B., Vinatier, S., Nixon, C.A., Fletcher, L., Howett, C., Calcutt, S.B., Bowles, N.E., Flasar, F.M., Taylor, F.W., 2007a. Oxygen compounds in Titan's stratosphere as observed by Cassini CIRS. Icarus 186, 354–363.

de Kok, R., Irwin, P.G.J., Teanby, N.A., Nixon, C.A., Jennings, D.E., Fletcher, L., Howett, C., Calcutt, S.B., Bowles, N.E., Flasar, F.M., Taylor, F.W., 2007b. Characteristics of Titan's stratospheric aerosols and condensate clouds from Cassini CIRS far-infrared spectra. Icarus 191, 223–235.

de Kok, R., Irwin, P.G.J., Teanby, N.A., Vinatier, S., Negrão, A., Osprey, S., Adriani, A., Moriconi, M.L.A.C., 2010. A tropical haze band in Titan's stratosphere. Icarus 207, 485–490.

Krasnopolsky, V.A., 2009. A photochemical model of titan's atmosphere and ionosphere. Icarus 201, 226–256.

Lacis, A.A., Oinas, V., 1991. A description of the correlated k distribution method for modeling nongray gaseous absorption, thermal emission, and multiple-scattering in vertically inhomogeneous atmospheres. Journal of Geophysical Research 96, 9027–9063.

Lavvas, P.P., Coustenis, A., Vardavas, I.M., 2008. Coupling photochemistry with haze formation in Titan's atmosphere, Part II: results and validation with Cassini/Huygens data. Planetary & Space Science 56, 67–99.

Lellouch, E., Vinatier, S., Moreno, R., Allen, M., Gulkis, S., Hartogh, P., Krieg, J.M., Maestrini, A., Mehdi, I., Coustenis, A., 2010. Sounding of Titan's atmosphere at submillimeter wavelengths from an orbiting spacecraft. Planetary & Space Science 58, 1724–1739.

Lide, D.R. (Ed.), 1995. CRC Handbook of Chemistry and Physics, 76th edition. CRC Press, Inc., Boca Raton.

Moreno, R., Lellouch, E., Lara, L.M., Courtin, R., Bockelée-Morvan, D., Hartogh, P., Rengel, M., Biver, N., Banaszkiewicz, M., González, A., 2011. First detection of hydrogen isocyanide (HNC) in Titan's atmosphere. Astronomy and Astrophysics 536, L12.

Moreno, R., Lellouch, E., Lara, L.M., Feuchtgruber, H., Rengel, M., Hartogh, P., Courtin, R., 2012. The abundance, vertical distribution and origin of H_2O in Titan's atmosphere: Herschel observations and photochemical modelling. Icarus 221, 753–767.

Niemann, H.B., Atreya, S.K., Demick, J.E., Gautier, D., Haberman, J.A., Harpold, D.N., Kasprzak, W.T., Lunine, J.I., Owen, T.C., Raulin, F., 2010. Composition of Titan's lower atmosphere and simple surface volatiles as measured by the Cassini–Huygens probe gas chromatograph mass spectrometer experiment. Journal of Geophysical Research 115, E12006.

Nixon, C.A., Achterberg, R.K., Teanby, N.A., Irwin, P.G.J., Flaud, J.M., Kleiner, I., Dehayem-Kamadjeu, A., Brown, L.R., Sams, R.L., Bézard, B., Coustenis, A., Ansty, T.M., Mamoutkine, A., Vinatier, S., Bjoraker, G.L., Jennings, D.E., Romani, P.N., Flasar, F.M., 2010. Upper limits for undetected trace species in the stratosphere of Titan. Faraday Discussions 147, 65–81.

Nixon, C.A., Jennings, D.E., Flaud, J.M., Bezard, B., Teanby, N.A., Irwin, P.G.J., Ansty, T.M., Coustenis, A., Vinatier, S., Flasar, F.M., 2009. Titan's prolific propane: the Cassini CIRS perspective. Planetary & Space Science 57, 1573–1585.

Pilbratt, G.L., Riedinger, J.R., Passvogel, T., Crone, G., Doyle, D., Gageur, U., Heras, A.M., Jewell, C., Metcalfe, L., Ott, S., Schmidt, M., 2010. Herschel space observatory. An ESA facility for far-infrared and submillimetre astronomy. Astronomy & Astrophysics 518, L1.

Press, W.H., Flannery, B.P., Teukolsky, S.A., Vetterling, W.T., 1992. Numerical Recipes, 2nd edition. Cambridge University Press, Cambridge, UK.

Rothman, L.S., Jacquemart, D., Barbe, A., Benner, D.C., Birk, M., Brown, L.R., Carleer, M.R., Chackerian, C., Chance, K., Coudert, L.H., Dana, V., Devi, V.M., Flaud, J.M., Gamache, R.R., Goldman, A., Hartmann, J.M., Jucks, K.W., Maki, A.G., Mandin, J.Y., Massie, S.T., Orphal, J., Perrin, A., Rinsland, C.P., Smith, M.A.H., Tennyson, J., Tolchenov, R.N., Toth, R.A., Vander Auwera, J., Varanasi, P., Wagner, G., 2005. The HITRAN 2004 molecular spectroscopic database. Journal of Quantitative Spectroscopy & Radiative Transfer 96, 139–204.

Swinyard, B.M., Ade, P., Baluteau, J.P., Aussel, H., Barlow, M.J., Bendo, G.J., Benielli, D., Bock, J., Brisbin, D., Conley, A., Conversi, L., Dowell, A., Dowell, D., Ferlet, M., Fulton, T., Glenn, J., Glauser, A., Griffin, D., Griffin, M., Guest, S., Imhof, P., Isaak, K., Jones, S., King, K., Leeks, S., Levenson, L., Lim, T.L., Lu, N., Makiwa, G., Naylor, D., Nguyen, H., Oliver, S., Panuzzo, P., Papageorgiou, A., Pearson, C., Pohlen, M., Polehampton, E., Pouliquen, D., Rigopoulou, D., Ronayette, S., Roussel, H., Rykala, A., Savini, G., Schulz, B., Schwartz, A., Shupe, D., Sibthorpe, B., Sidher, S., Smith, A.J., Spencer, L., Trichas, M., Triou, H., Valtchanov, I., Wesson, R., Woodcraft, A., Xu, C.K., Zemcov, M., Zhang, L., 2010. In-flight calibration of the Herschel-SPIRE instrument. Astronomy & Astrophysics 518, L4.

Teanby, N.A., 2007. Constrained smoothing of noisy data using splines in tension. Mathematical Geology 39, 419–434.

Teanby, N.A., Fletcher, L.N., Irwin, P.G.J., Fouchet, T., Orton, G.S., 2006a. New upper limits for hydrogen halides on Saturn derived from Cassini-CIRS data. Icarus 185, 466–475.

Teanby, N.A., Irwin, P.G.J., 2007. Quantifying the effect of finite field-of-view size on radiative transfer calculations of Titan's limb spectra measured by Cassini-CIRS. Astrophysics and Space Science 310, 293–305.

Teanby, N.A., Irwin, P.G.J., de Kok, R., Jolly, A., Bézard, B., Nixon, C.A., Calcutt, S.B., 2009a. Titan's stratospheric C_2N_2, C_3H_4, and C_4H_2 abundances from Cassini/CIRS far-infrared spectra. Icarus 202, 620–631.

Teanby, N.A., Irwin, P.G.J., de Kok, R., Nixon, C.A., 2009b. Dynamical implications of seasonal and spatial variations in Titan's stratospheric composition. Philosophical Transactions of the Royal Society of London A 367, 697–711.

Teanby, N.A., Irwin, P.G.J., de Kok, R., Nixon, C.A., Coustenis, A., Royer, E., Calcutt, S.B., Bowles, N.E., Fletcher, L., Howett, C., Taylor, F.W., 2008a. Global and temporal variations in hydrocarbons and nitriles in Titan's stratosphere for northern winter observed by Cassini/CIRS. Icarus 193, 595–611.

Teanby, N.A., Irwin, P.G.J., de Kok, R., 2010a. Compositional evidence for Titan's stratospheric tilt. Planetary & Space Science 58, 792–800.

Teanby, N.A., Irwin, P.G.J., de Kok, R., Nixon, C.A., 2010b. Mapping Titan's HCN in the far infra-red: implications for photochemistry. Faraday Discussions 147, 51–64.

Teanby, N.A., Irwin, P.G.J., de Kok, R., Nixon, C.A., 2010c. Seasonal changes in Titan's polar trace gas abundance observed by Cassini. Astrophysical Journal 724, L84–L89.

Teanby, N.A., Irwin, P.G.J., deKok, R., Nixon, C.A., Coustenis, A., Bézard, B., Calcutt, S.B., Bowles, N.E., Flasar, F.M., Fletcher, L., Howett, C., Taylor, F.W., 2006b. Latitudinal variations of HCN, HC_3N, and C_2N_2 in Titan's stratosphere derived from Cassini CIRS data. Icarus 181, 243–255.

Teanby, N.A., Irwin, P.G.J., de Kok, R., Vinatier, S., Bézard, B., Nixon, C.A., Flasar, F.M., Calcutt, S.B., Bowles, N.E., Fletcher, L., Howett, C., Taylor, F.W., 2007. Vertical profiles of HCN, HC_3N, and C_2H_2 in Titan's atmosphere derived from Cassini/CIRS data. Icarus 186, 364–384.

Teanby, N.A., de Kok, R., Irwin, P.G.J., Osprey, S., Vinatier, S., Gierasch, P.J., Read, P.L., Flasar, F.M., Conrath, B.J., Achterberg, R.K., Bezard, B., Nixon, C.A., Calcutt, S.B., 2008b. Titan's winter polar vortex structure revealed by chemical tracers. Journal of Geophysical Research 113, E12003.

Tomasko, M.G., Doose, L., Engel, S., Dafoe, L.E., West, R., Lemmon, M., Karkoschka, E., See, C., 2008. A model of Titan's aerosols based on measurements made inside the atmosphere. Planetary & Space Science 56, 669–707.

Vinatier, S., Bézard, B., Fouchet, T., Teanby, N.A., de Kok, R., Irwin, P.G.J., Conrath, B.J., Nixon, C.A., Romani, P.N., Flasar, F.M., Coustenis, A., 2007. Vertical abundance profiles of hydrocarbons in Titan's atmosphere at 15°S and 80°N retrieved from Cassini/CIRS spectra. Icarus 188, 120–138.

Vinatier, S., Bézard, B., Nixon, C.A., Mamoutkine, A., Carlson, R.C., Jennings, D.E., Guandique, E.A., Teanby, N.A., Bjoraker, G.L., Flasar, F.M., Kunde, V.G., 2010. Analysis of Cassini/CIRS limb spectra of Titan acquired during the nominal mission I. hydrocarbons, nitriles and CO_2 vertical mixing ratio profiles. Icarus 205, 559–570.

Vuitton, V., Yelle, R.V., Lavvas, P., 2009. Composition and chemistry of Titan's thermosphere and ionosphere. Philosophical Transactions of the Royal Society of London A 367, 729–741.

Vuitton, V., Yelle, R.V., McEwan, M.J., 2007. Ion chemistry and N-containing molecules in Titan's upper atmosphere. Icarus 191, 722–742.

Waite, J.H., Niemann, H., Yelle, R.V., Kasprzak, W.T., Cravens, T.E., Luhmann, J.G., McNutt, R.L., Ip, W.H., Gell, D., De La Haye, V., Muller-Wordag, I., Magee, B., Borggren, N., Ledvina, S., Fletcher, G., Walter, E., Miller, R., Scherer, S., Thorpe, R., Xu, J., Block, B., Arnett, K., 2005. Ion neutral mass spectrometer results from the first flyby of Titan. Science 308, 982–986.

Wilson, E.H., Atreya, S.K., 2004. Current state of modeling the photochemistry of Titan's mutually dependent atmosphere and ionosphere. Journal of Geophysical Research 109, E06002.

Wilson, T.L., Rohlfs, K., Hüttemeister, S., 2009. Tools of Radio Astronomy, 5th edition Springer-Verlag, Berlin.

Wishnow, E.H., Orton, G.S., Ozier, I., Gush, H.P., 2007. The distortion dipole rotational spectrum of CH_4: a low temperature far-infrared study. Journal of Quantitative Spectroscopy & Radiative Transfer 103, 102–117.

Yelle, R.V., Vuitton, V., Lavvas, P., Klippenstein, S.J., Smith, M.A., Hörst, S.M., Cui, J., 2010. Formation of NH_3 and CH_2NH in Titan's upper atmosphere. Faraday Discussions 147, 31–49.